Inorg. Chem. **2007**, *46*, 4575–4582

Inorganic Chemistry
Article

Influence of Oxygen Defects on the Crystal Structure and Magnetic Properties of the $(Tb_{1-x}Na_x)MnO_{3-y}$ ($0 \leq x \leq 0.3$) System

T. S. Chan,[†] R. S. Liu,*[,†] C. C. Yang,[‡,§] W.-H. Li,[‡,§] Y. H. Lien,[||] C. Y. Huang,[⊥] Jeff W. Lynn,[#] J. M. Chen,[£] and H.-S. Sheu[£]

Department of Chemistry and Center for Nano Storage Research, National Taiwan University, Taipei 106, Taiwan, Institute of Physics, Academia Sinica, Taipei 115, Taiwan, Department of Physics, National Central University, Chung-Li 320, Taiwan, Institute of Materials Manufacturing, Chinese Culture University, Taipei 111, Taiwan, Institute of Optoelectronic Science and Technology, National Taiwan Normal University, Taipei 106, Taiwan, NIST Center for Neutron Research, NIST, Gaithersburg, Maryland 20899-8562, and National Synchrotron Radiation Research Center, Hsinchu 300, Taiwan

Received January 31, 2007

The crystallographic and magnetic behaviors of $(Tb_{1-x}Na_x)MnO_{3-y}$ ($0 \leq x \leq 0.3$) have been studied by neutron powder diffraction (NPD), synchrotron X-ray powder diffraction, and Raman spectroscopy techniques. Although Na^+ ions have larger ionic radii than Tb^{3+} ions, analysis of NPD data reveals a decrease in cell volume upon Na-doping, which can be explained solely by the occurrence of oxygen deficiencies and not by the size effect. The Raman spectrum represents the variation in bond length and bond angle, which originates from the balance of ions, asymmetric structure, and defects in the system. Na-doping causes an oxygen deficiency, and consequently, a peak shift is seen in the Raman spectrum because of the structural adjustment resulting from the doping. The observed effective moments decrease with increasing x because of the replacement of Tb^{3+} ions by Na^+ ions. The well-defined peak at ~45 K (labeled T_{Mn}) of the $x = 0.3$ sample is associated with Mn spin ordering, while the magnetic responses associated with T_{Mn} are not clearly present in the $x = 0.15$ and $x = 0$ samples.

1. Introduction

Multiferroic materials with the coexistence of (anti)-ferromagnetic and (anti)ferroelectric properties have been intensively studied in recent years. The mixed oxides of rare earth and manganese, for example, $TbMnO_3$,[1] $YMnO_3$,[2] $BiMnO_3$[3] and $TbMn_2O_5$,[4] display a great variety of magnetic structures and charge-ordering phenomena. Among these mixed oxides, the evolution of magnetic and structural properties have been reported in polycrystalline $(Tb_{1-x}^{3+}Ca_x^{2+})$-MnO_3[5] and single-crystal $(Tb_{1-x}^{3+}Gd_x^{3+})MnO_3$[6] systems. In the case of doped $TbMnO_3$, the chemical substitution of Tb^{3+} by alkali metal with a formal oxidation state of +1 would be expected to induce more holes in the system and cause an increase in the formal Mn valences. This approach can provide helpful information on the role of the valence of Mn and also about the role of structural change with substitution.[7−11]

Recently, we synthesized $(Tb_{1-x}Na_x)MnO_3$ perovskites and studied their crystal structure and electrical properties. We found that the activation energy and resistivity decreased with

* To whom correspondence should be addressed. E-mail: rsliu@ntu.edu.tw.
† National Taiwan University.
‡ Academia Sinica.
§ National Central University.
|| Chinese Culture University.
⊥ National Taiwan Normal University.
NIST Center for Neutron Research.
£ National Synchrotron Radiation Research Center.

(1) Kimura, T.; Koto, T.; Shintani, H.; Ishizaka, K.; Arima, T.; Tokura, Y. *Nature* **2003**, *426*, 55.
(2) Van Aken, B. B.; Palstra, T. T. M.; Filippetti, A.; Spaldin, N. A. *Nat. Mater.* **2004**, *3*, 164.
(3) Kimura, T.; Kawamoto, S.; Yamada, I.; Azuma, M.; Takano, M.; Tokura, Y. *Phys. Rev. B.* **2003**, *67*, 180401.
(4) Hur, N.; Park, S.; Sharma, P. A.; Ahn, J. S.; Guha, S.; Cheong, S.-W. *Nature* **2004**, *429*, 392.
(5) Blasco, J.; Ritter, C.; García, J.; Teresa, J. M.; Perez-Cacho, J.; Ibarra, M. R. *Phys. Rev. B.* **2000**, *62*, 5609.
(6) Goto, T.; Yamasaki, Y.; Watanabe, H.; Kimura, T.; Tokura, Y. *Phys. Rev. B.* **2005**, *72*, 220403.
(7) Singh, R. N.; Shivakumara, C.; Vasanthacharya, N. Y.; Subramanian, S.; Hegde, M. S.; Rajagopal, H.; Sequeira, A. *J. Solid State Chem.* **1998**, *19*, 137.
(8) Boix, T.; Sapina, F.; Fadli, Z. E.; Martinez, E.; Beltran, A.; Vergara, J.; Ortega, R. J.; Rao, K. V. *Chem. Mater.* **1998**, *10*, 1569.
(9) McCarrol, W. H.; Fawcett, I. D.; Greenblatt, M.; Ramanujachary, K. V. *J. Solid State Chem.* **1999**, *146*, 88.

10.1021/ic070190f CCC: $37.00
Published on Web 05/02/2007

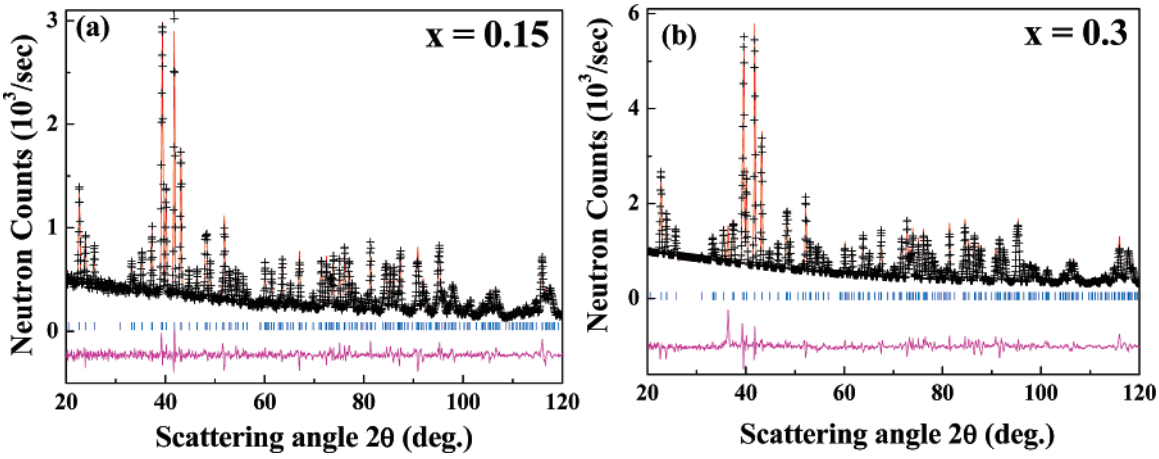

Figure 1. Observed (crosses), calculated (solid line), and differences (bottom) NPD Rietveld profiles of $(Tb_{1-x}Na_x)MnO_{3-y}$ for (a) $x = 0.15$ and (b) 0.3 at 300 K. Bragg reflections are indicated by tick marks.

increasing Na content.[12] In addition, we also reported that oxygen content can affect the magnetic structures of both Mn and Tb in $TbMnO_3$.[13] The modulated spin structure of the Mn moments was found to reappear in systems with high Na doping. However, the low-temperature crystallographic behaviors and electron structure properties are still unclear in Na-doped system because of a partial oxygen deficiency.

On the other hand, Raman spectroscopy is a powerful tool for the study of structural disorders, including the dynamic processes. There have been numerous reports on the variations of the Raman spectra of $(R_{1-x}^{3+}A_x^{2+})MnO_3$ perovskites (R = rare earth; A = Ca, Sr, Ba; $0 < x < 1$) with increasing x values and temperature.[14−19] As demonstrated, the Raman spectra of doped manganites consist of two or three broad bands at positions close to those of the strongest Raman lines for the parent orthorhombic $RMnO_3$ compounds with *Pnma* structure. Furthermore, the disorder in the doped rare-earth manganites varies strongly with doping level and temperature. Although the role of lattice distortions in the interplay of magnetic and transport properties of $(R_{1-x}^{3+}A_x^{2+})MnO_3$ is widely recognized, to our knowledge, no experimental reports about Na-doped $TbMnO_3$ under various temperatures have been published.

In this work, we investigated the crystallographic behaviors of $(Tb_{1-x}Na_x)MnO_{3-y}$ ($0 \le x \le 0.3$) by a combination of neutron powder diffraction (NPD), synchrotron X-ray powder diffraction, and Raman spectroscopy. The electronic structure from X-ray absorption spectra (XAS) measurements at the Mn K-edge and O K-edge is also reported. The influence of oxygen deficiency on the structure and magnetic properties of $(Tb_{1-x}^{3+}Na_x^{+})MnO_{3-y}$ will be discussed.

2. Experimental Section

Polycrystalline samples of $(Tb_{1-x}Na_x)MnO_{3-y}$ ($0 \le x \le 0.3$) were synthesized by conventional solid-state reaction. Detailed sample preparation is described elsewhere.[12] High-resolution neutron powder diffraction (NPD) patterns were collected on the BT-1 with $\lambda = 1.5401$ Å , a 32-detector powder diffractometer at the NIST Center for Neutron Research, employing a Cu(311) monochromator crystal and 15′-20′-7′ FWHM angular collimations. Raman spectra were recorded on a Jobin Yvon T64000 spectrometer in the back-scattering mode, employing a 514.5 nm line from an Ar^+ laser as the excitation line with an input power of 0.5 mW (at the focus spot, 2−3 μm in diameter). A nitrogen cryostat pump was used to control the sample temperature, and sufficient time was allowed for each temperature change. Smooth top and bottom surface and thin-pellet powder samples were used to reduce diffuse scattering and temperature differences and to collect all Raman modes simultaneously.

The O K-edge X-ray absorption near-edge structure (XANES) measurements were performed at a 6 m high-energy spherical grating monochromator (HSGM) beamline at the National Synchrotron Radiation Research Center (NSRRC) in Taiwan. The absorption spectra were recorded in the X-ray fluorescence-yield (FY) mode using a microchannel plate (MCP) detector consisting of a dual set of MCPs with an electrically isolated grid mounted in front of them. The grid was set to a voltage of 100 V, the front of the MCPs to −2000 V, and the rear to −200 V. The grid bias ensured that positive ions did not enter the detector, while the MCP bias ensured that no electrons were detected. The detector was located parallel to the sample surface at a distance of ∼2 cm. Photons were incident at an angle of 45° with respect to the sample normal. The incident photon flux was monitored simultaneously

(10) Sahana, M.; Singh, R. N.; Shivakumara, C.; Vasanthacharya, N. Y.; Hegde, M. S.; Subramanian, S.; Prasad, V.; Subramanyam, S. V. *Appl. Phys. Lett.* **1997**, *70*, 2909.
(11) Wang, X. L.; Kennedy, S. J.; Gehringer, P.; Lang, W.; Liu, H. K.; Dou, S. X. *J. Appl. Phys.* **1998**, *83*, 7177.
(12) Chan, T. S.; Liu, R. S.; Lien, Y. H.; Yang, C. C.; Huang, C. Y.; Lin, J. G. *IEEE Trans. Magn.* **2005**, *41*, 2751.
(13) Yang, C. C.; Chung, M. K.; Chan, T. S.; Liu, R. S.; Lien, Y. H.; Huang, C. Y.; Chan, Y. Y. Yao, Y. D.; Lynn, J. W. *Phys. Rev. B.* **2006**, *74*, 094409.
(14) Iliev, M. N.; Litvinchuk, A. P.; Abrashev, M. V.; Ivanov, V. G.; Lee, H. G.; McCarrol, W. H.; Greenblatt, M.; Meng, R. L.; Chu, C. W. *Phys. C* **2000**, *341*, 2257.
(15) Singh, R. N.; Shivakumara, C.; Vasanthacharya, N. Y.; Subramanian, S.; Hegde, M. S.; Rajagopal, H.; Sequeira, A. *J. Solid State Chem.* **1998**, *19*, 137.
(16) Boix, T.; Sapina, F.; Fadli, Z. E.; Martinez, E.; Beltran, A.; Vergara, J.; Ortega, R. J.; Rao, K. V. *Chem. Mater.* **1998**, *10*, 1569.
(17) McCarrol, W. H.; Fawcett, I. D.; Greenblatt, M.; Ramanujachary, K. V. *J. Solid State Chem.* **1999**, *146*, 88.
(18) Sahana, M.; Singh, R. N.; Shivakumara, C.; Vasanthacharya, N. Y.; Hegde, M. S.; Subramanian, S.; Prasad, V.; Subramanyam, S. V. *Appl. Phys. Lett.* **1997**, *70*, 2909.
(19) Wang, X. L.; Kennedy, S. J.; Gehringer, P.; Lang, W.; Liu, H. K.; Dou, S. X. *J. Appl. Phys.* **1998**, *83*, 7177.

Table 1. Refined Atomic Positions, Isotropic Thermal Factors, Occupancies, and Reliability Factors of $(Tb_{1-x}Na_x)MnO_{3-y}$ in Orthorhombic *Pbnm* Space Group from Neutron Diffraction Data at 300 K[a]

		$x = 0$	$x = 0.1$	$x = 0.15$	$x = 0.2$	$x = 0.3$
a (Å)		5.2996(2)	5.2987(2)	5.2985(2)	5.2980(3)	5.2960(2)
b (Å)		5.8503(2)	5.8095(2)	5.7776(3)	5.7496(3)	5.7417(3)
c (Å)		7.4013(2)	7.4106(3)	7.4152(3)	7.4249(4)	7.4257(3)
V (Å^3)		229.47(1)	228.12(2)	226.96(2)	226.17(2)	225.80(2)
s		0.099	0.092	0.087	0.082	0.081
Tb	4c (x, y, 1/4)					
x		−0.01634(3)	−0.01687(3)	−0.0165(40	−0.0146(5)	−0.0137(4)
y		0.08112(2)	0.07906(2)	0.07802(3)	0.0772(4)	0.0763(4)
U_{iso} (Å^2)		0.55(3)	0.57(4)	0.75(4)	0.95(6)	0.76(5)
occupancy (Tb)		1	0.9	0.85	0.8	0.7
occupancy (Na)		0	0.1	0.15	0.2	0.3
Mn	4b (1/2, 0, 0)					
U_{iso} (Å^2)		0.45(5)	0.67(6)	0.61(7)	0.36(9)	0.50(7)
O(1)	4c (x, y, 1/4)					
x		0.1054(3)	0.1038(4)	0.1031(5)	0.1027(5)	0.1025(4)
y		0.4659(3)	0.4664(32)	0.4667(4)	0.4642(5)	0.4639(4)
U_{iso} (Å^2)		0.72(4)	0.67(6)	0.74(8)	0.77(9)	0.87(7)
occupancy O(1)		1	0.985(7)	0.936(9)	0.925(7)	0.893(8)
O(2)	8d (x, y, z)					
x		−0.2963(2)	−0.2968(3)	−0.2966(4)	−0.2970(4)	−0.2975(3)
y		0.3272(2)	0.3247(3)	0.3227(3)	0.3203(4)	0.3201(3)
z		0.0507(2)	0.0511(2)	0.0500(3)	0.0517(3)	0.0519(2)
occupancy O(2)		1	0.971(7)	0.957(9)	0.937(7)	0.904(8)
occupancy O total		3	2.900(2)	2.850(7)	2.799(2)	2.701(2)
U_{iso} (Å^2)		0.70(2)	0.89(3)	1.03(4)	0.98(5)	1.03(4)
R_p/R_{wp} (%)		4.49/5.73	4.61/6.34	5.76/7.73	6.52/9.02	5.26/7.38
χ^2		1.07	2.42	1.94	4.75	3.40

[a] The strain parameter is defined as $s = 2(b - a)/(a + b)$.

Table 2. Selected Tb−O, Mn−O Distances (Å), and Mn−O−Mn Angles for the Refinements of $(Tb_{1-x}Na_x)MnO_{3-y}$ in Orthorhombic *Pbnm* Space Group from Neutron Diffraction Data at 300 K[a]

	$x = 0$	$x = 0.1$	$x = 0.15$	$x = 0.2$	$x = 0.3$
Tb−O(1)$_{av}$ (×2)	2.3106(2)	2.3116(2)	2.3077(3)	2.2940(4)	2.2908(3)
Tb−O(2)$_{av}$ (×6)	2.4753(2)	2.4733(2)	2.4734(3)	2.4739(3)	2.4742(2)
Mn−O(1) (×2)	1.9431(5)	1.9426(6)	1.9423(7)	1.9453(8)	1.9456(7)
Mn−O(2) (×2)	2.2294(2)	2.2051(2)	2.1851(2)	2.1667(2)	2.1620(2)
Mn−O(2) (×2)	1.9049(2)	1.9110(2)	1.9117(2)	1.9213(2)	1.9237(2)
Mn−O(2)$_{av}$ (×4)	2.0672(2)	2.0581(2)	2.0484(2)	2.0440(2)	2.0429(2)
ΔMn−O(2)	0.3245	0.2941	0.2734	0.2454	0.2383
Mn−O(1)/Mn−O(2)$_{av}$	0.940	0.943	0.948	0.951	0.952
Mn−O$_{av}$ (×6)	2.0258(3)	2.0196(3)	2.0130(4)	2.0111(4)	2.0104(4)
Mn−O(1)−Mn	144.44(9)	145.00(1)	145.27(1)	145.19(2)	145.21(1)
Mn−O(2)−Mn	180.0	180	179.96(0)	179.96(0)	179.98(0)
T_C (K)	−12(2)	−30 (1)	−4(3)	−21(1)	−21(2)
C (emu g^{-1} Oe K)	5.46(3) × 10^{-2}	5.36(3) × 10^{-2}	5.65(9) × 10^{-2}	5.06(3) × 10^{-2}	4.77(2) × 10^{-2}
μ_{eff} (fit) (μ_B/fu)	10.7(3)	10.4(1)	10.4(7)	9.7(1)	9.1(2)

[a] Some physical parameters obtained from the Curie−Weiss fits are also given.

by a Ni mesh located after the exit slit of the monochromator. The photon energies were calibrated with an accuracy of 0.1 eV using the O K-edge absorption peak at 530.1 eV of a CuO reference.

The Mn K-edge XANES were recorded in transmission mode for the synthesized powder, mounted on Scotch tape, at a BL17C Wiggler beamline using a double-crystal Si (111) monochromator. The X-ray high harmonic was rejected by mirrors. The ion chambers used for measuring the incident (I_0) and transmitted (I) beam intensities were filled with a mixture of N_2 and H_2 gases and a mixture of N_2 and Ar gases, respectively. Energy calibration was carried out by using the first inflection point of the Mn K-edge (6539 eV) absorption spectrum of Mn metal foil as a reference. Reference spectra were simultaneously collected for each in situ spectrum using Mn metal foils.

Synchrotron XRD patterns were taken with a large Debye−Scherrer camera installed at the BL01C2 beam line of NSRRC with $\lambda = 0.516606$ Å. The sample was contained in a glass capillary tube with an inner diameter of 0.1 mm and was rotated during measurements. The synchrotron XRD data were collected in a 2θ range from 0.08 to 28° with a step interval of 0.01°. Structural refinements were made for both the X-ray and neutron diffractograms using the GSAS program.[20] Magnetic susceptibilities were carried out between 5 and 300 K by a commercial Quantum Design (PPMS) magnetometer with an ac experimental setup.

3. Results and Discussion

Figure 1a and b shows experimental, calculated, and difference NPD patterns for $(Tb_{1-x}Na_x)MnO_{3-y}$ ($x = 0.15$, 0.3) at 300 K with $\lambda = 1.5401$ Å. All the observed peaks can be fitted with the reflection conditions in the orthorhombic *Pbnm* space group. The final structural parameters are given in Table 1, and selected bond length and angles

(20) Larson, A. C.; Von Dreele, R. B. *Generalized Structure Analysis System (GSAS)*; Los Alamos National Laboratory Report LAUR 86-748; Los Alamos National Laboratory: Los Alamos, NM, 1994.

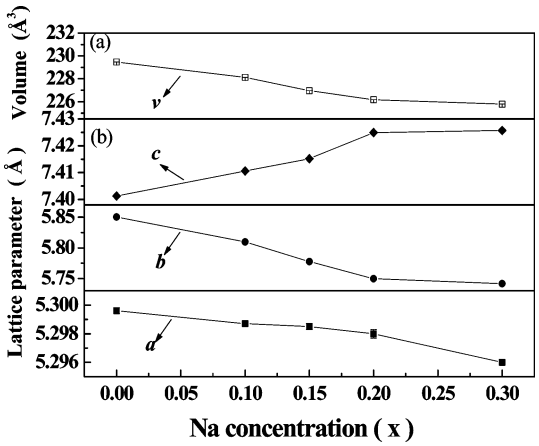

Figure 2. Lattice parameters and unit cell volume as a function of Na concentration. Error bars are smaller than the symbol size.

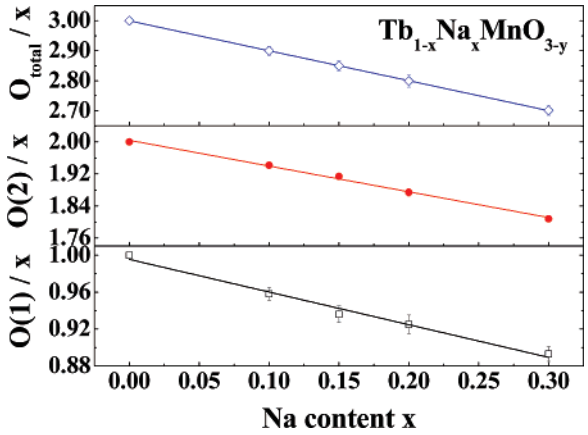

Figure 3. NPD Rietveld of oxygen occupancy as a function of Na concentration. Some error bars are smaller than the symbol size.

are listed in Table 2. As seen from Table 1, Rietveld analysis afforded sufficiently low R factors. At 300 K, the lattice parameters, as well as the unit cell volume, are plotted as a function of Na concentration in Figure 2. It is worth mentioning that the changes in the lattice parameters and unit cell volume were anisotropic. The decrease in the two basal plane lattice parameters (*a* and *b* axes), together with an increase in the axial one (*c* axis), results in the cell volume becoming smaller (by ~2% from $x = 0$ to 0.3). It is well-known that the ionic radius of Na^+ is larger (1.18 Å) than that of Tb^{3+} (1.04 Å).[21] Therefore, the decrease in cell volume upon Na-doping can be explained by the occurrence of oxygen deficiencies and is not caused by the size effect.

In Figure 3, the NPD Rietveld of oxygen occupancy is plotted as a function of Na concentration. As noted, the Na-free $TbMnO_{3-y}$ sample is essentially oxygen-stoichiometric, that is, $3-y \approx 3.0$, which is in good agreement with Kitayama's report.[22] When Na content increases, the total oxygen occupancy decreases from 3.0 ($x = 0$) to 2.7 ($x = 0.3$). Furthermore, the bond valence sum calculated from the refined structure parameters shows that the Mn ions in all of the samples are trivalent. These results indicated that the

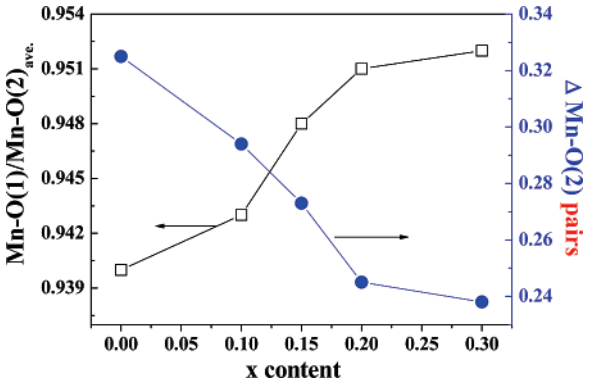

Figure 4. Ratio of $Mn-O(1)/Mn-O(2)_{av}$ and differences between the Mn−O(2) bond pairs (ΔMn−O(2)) as a function of Na concentration of $(Tb_{1-x}Na_x)MnO_{3-y}$.

concomitant decrease in oxygen content in Na-substituted $(Tb_{1-x}Na_x)MnO_{3-y}$ samples counterbalances the substitution effect of monovalent Na ions for trivalent Tb ions. Similar results have also been found for the $(La,Na)MnO_{3-\delta}$ systems.[23−24]

The effect of Na doping on local octahedral MnO_6 in $(Tb_{1-x}Na_x)MnO_{3-y}$ is studied on the basis of the bond length variation. As noted in Table 2 and Figure 4, the ratio of apical Mn−O(1) bond to the average equatorial Mn−O(2) increases from 0.939 ($x = 0$) to 0.952 Å ($x = 0.3$) with increasing Na content. Moreover, the differences between the Mn−O(2) bond pairs decreases from 0.3245 ($x = 0$) to 0.2383 Å ($x = 0.3$). These tests of the octahedral distortion indicate that the MnO_6 coordination is actually more regular in the doped samples. Furthermore, the spontaneous orthorhombic strain, defined as $s = 2(b - a)/(a + b)$, which also is a measure of the distortion of the octahedral, increases as a result of octahedral tilting.[25] As shown in Table 1, the *s* value (0.099) of $TbMnO_3$ is in agreement with the early report by Alonso et al. ($s = 0.098$),[26] which also showed an increase of the Jahn−Teller (JT) effect, observed from La to Tb. In our case, the *s* value decreases with increasing Na content, which indicates the reduction in the octahedral distortion and JT effect.

X-ray absorption spectroscopy (XAS) has been employed to probe the electronic and local structure of transition metal ions. The absorption features of the transition metal K-edge XAS provide useful structural information, such as the oxidation states of chemical species, their site symmetries, and covalent bond strengths.[27−31] We now discuss the formal

(21) Shannon, R. D. *Acta. Crystallogr. A* **1976**, *32*, 751.
(22) Kitayama, K.; Kobayashi, M.; Takano. H.; Nambu, N.; Hirasawa, H. *J. Solid State Chem.* **2003**, *176*, 151.
(23) McCarroll, W. H.; Fawcett, I. D.; Greenblatt, M.; Ramanujachary, K. V. *J. Solid State Chem.* **1999**, *146*, 88.
(24) Singh, R. N.; Shivakumara, D.; Vasanthacharya, N. Y.; Subramanian, S.; Hegde, M. S.; Rajagopal, H.; Sequeira, A. *J. Solid State Chem.* **1998**, *137*, 19.
(25) Woodward, P. M.; Vogt, T.; Cox, D. E.; Arulraj, A.; Rao, C. N. R.; Karen, P.; Cheetharm, A. K. *Chem. Mater.* **1998**, *10*, 3652.
(26) Alonso, J. A.; Martinez-Lope, M. J.; Casais, M. T.; Fereundez-Diaz, M. T. *Inorg. Chem.* **2000**, *39*, 917.
(27) Croft, M.; Sill, D.; Greenblatt, M.; Lee, C.; Cheong, S.-W.; Ramanujachary, K. V.; Tran, D. *Phys. Rev. B* **1997**, *55*, 8726.
(28) Zeng, Z.; Greenbaltt, M.; Croft, M. *Phys. Rev. B* **1999**, *59*, 8784.
(29) Ignatov, A.; Yu Ali, N.; Khalid, S. *Phys. Rev. B* **2001**, *63*, 014413-1.
(30) Bondino, F.; Plate, M.; Zangrando, M.; Zacchigna, M.; Cocco, D.; Comin, A.; Alessandri, I.; Malavasi, L.; Parmigiani, F. *J. Phys. Chem. B* **2004**, *108*, 4018.

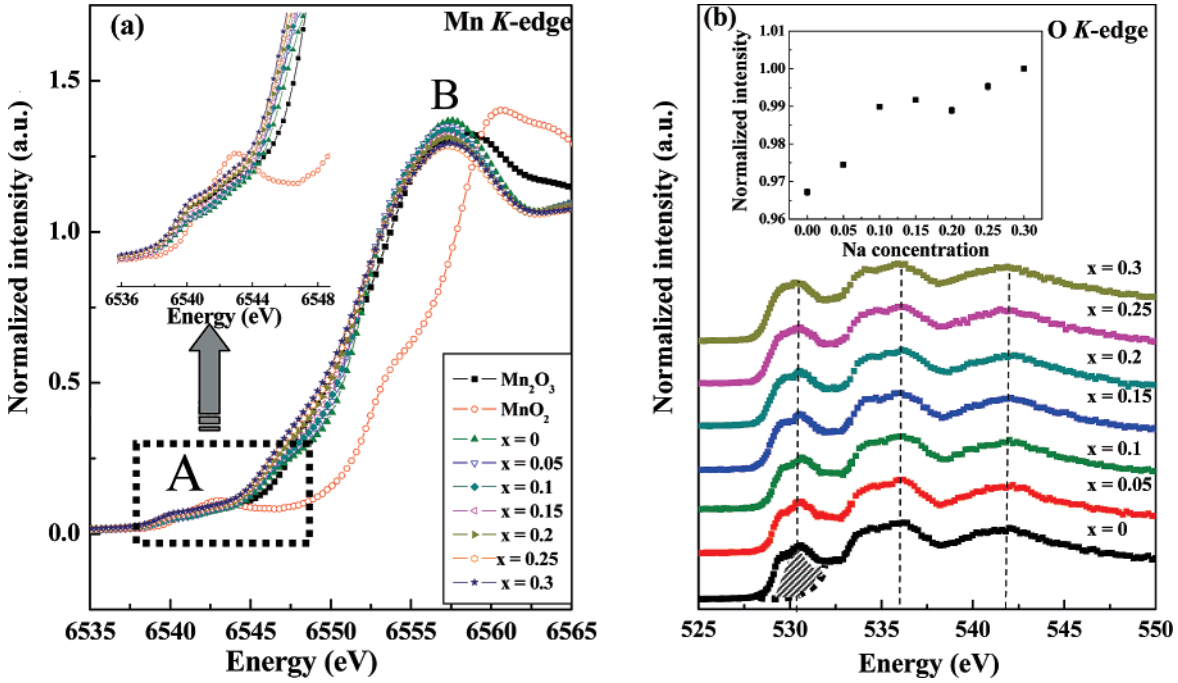

Figure 5. (a) Mn K-edge XANES spectra of $(Tb_{1-x}Na_x)MnO_{3-y}$ along with two standards of Mn_2O_3 (Mo^{3+}) and MnO_2 (Mn^{4+}) for comparison. (b) O K-edge XANES spectra of $(Tb_{1-x}Na_x)MnO_{3-y}$. Variations of pre-edge peak intensity of the O K-edge absorption spectra of $(Tb_{1-x}Na_x)MnO_{3-y}$ are given in the inset.

Mn valence of $(Tb_{1-x}Na_x)MnO_{3-y}$. The Mn K-edge XANES spectra of $(Tb_{1-x}Na_x)MnO_{3-y}$ are shown in Figure 5a, along with two standards, Mn_2O_3 (Mn^{3+}) and MnO_2 (Mn^{4+}), for comparison. The weak pre-edge peak labeled A emerges from the 1s → 3d transitioncaused by pure electric quadrupole coupling or 3d−4p orbital mixing arising from the noncentrosymmetric environment of the slightly distorted octahedral site in the orthorhombic *Pbnm* space group. The main absorption features labeled B are ascribed to the pure dipole-allowed 1s → 4p transition. As the Na content increases, the Mn K-edge XANES spectrum shows systematic changes in the shape and intensity of pre-edge peaks. Especially noteworthy is that peak B does not show a clear shift to higher energy values. The energy position and shape of these absorption features are very similar to those of Mn_2O_3 standard compounds. This indicates that the valency of Mn ions in $(Tb_{1-x}Na_x)MnO_{3-y}$ remains nearly 3+ with increasing Na content.

So far, we have demonstrated that an increase of Na content in $(Tb_{1-x}Na_x)MnO_{3-y}$ leads to a reduction in activation energy from 62 ($x = 0$) to 39 meV ($x = 0.3$).[12] Here, we examine the detailed electronic structure features. In principle, the positions and intensities of pre-edge peaks in the O K-edge XANES spectra provide significant structural information about the chemical bonding between the ligand and metal atoms.[32] Figure 5b shows the O K-edge XANES spectra of $(Tb_{1-x}Na_x)MnO_{3-y}$, which exhibit the pre-edge peaks centered at ~530.6 eV, the double peaks at ~535 eV, and a broad structure at ~542 eV. The pre-edge peaks below

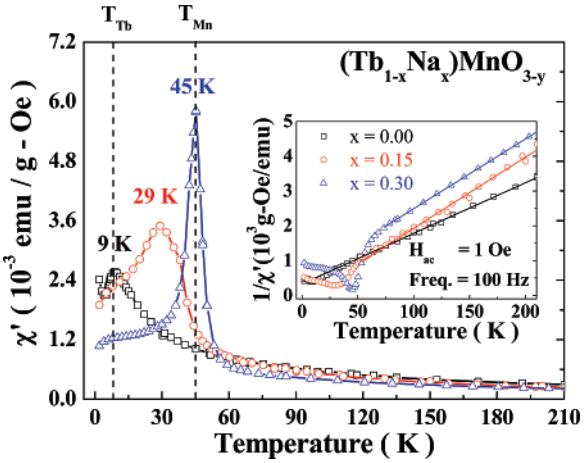

Figure 6. Temperature dependence of the magnetic susceptibility (χ') of $(Tb_{1-x}Na_x)MnO_{3-y}$ ($x = 0$, 0.15, and 0.3). Inverse susceptibility ($1/\chi'$) is also shown in the inset. The oscillating magnetic field has an amplitude of 1 Oe and a frequency of 100 Hz.

531.1 eV of the O K-edge absorption spectra correspond to the transition of the oxygen 1s electron to the hybridized state of Mn 3d and oxygen 2p orbitals, whereas the broad peaks above 542 eV correspond to the transitions to hybridized states of oxygen 2p and Mn 4sp orbitals. As noted, the pre-edge peak position remains nearly constant throughout all Na concentrations. The variation of the integrated intensity of the pre-edge peak of $(Tb_{1-x}Na_x)MnO_{3-y}$ gives important information on the hole distribution on Mn−O sites because the density of an unoccupied state is related to the hybridization of Mn 3d-O 2p orbitals. The shaded area in Figure 5b is the integrated pre-edge intensity corresponding to an oxygen 2p orbital hybridized with a Mn 3d band. The variations of normalized integrated intensity of the pre-edge region of the O K-edge XANES spectra of $(Tb_{1-x}Na_x)MnO_{3-y}$

(31) Ghgna, P.; Carollo, A.; Flor, G.; Malavasi, L.; Peruga, G. S. *J. Phys. Chem. B* **2005**, *109*, 4365.
(32) Yoon, W. S.; Balasubrmanian, M.; Chung, K. Y.; Yang, Z. Q.; McBreen, J.; Grey, C. P.; Fischer, D. A. *J. Am. Chem. Soc.* **2005**, *127* (49), 17479.

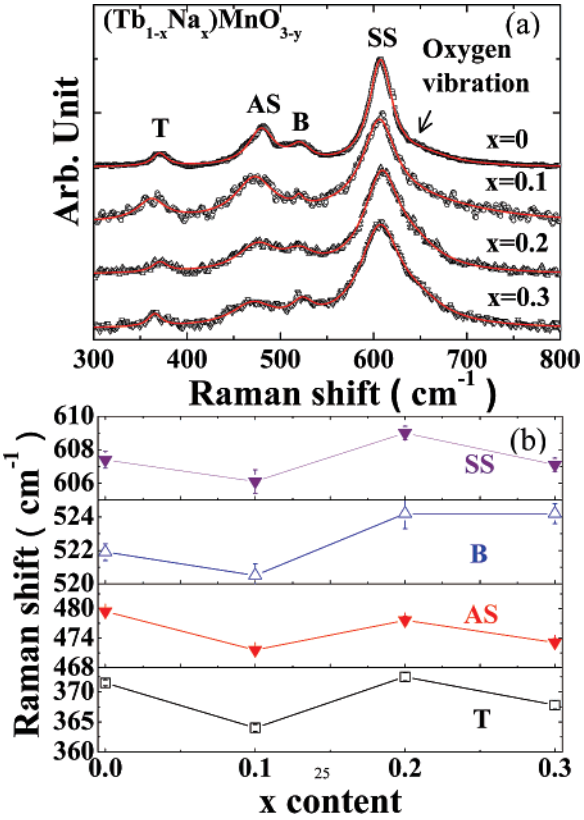

Figure 7. (a) Raman spectrum of $(Tb_{1-x}Na_x)MnO_{3-y}$ ($x = 0$, 0.1, 0.2, and 0.3) at 300 K. (b) Raman shift as a function of Na concentration.

Table 3. Raman Shifts Identified of $(Tb_{1-x}Na_x)MnO_{3-y}$ ($x = 0$, 0.1, 0.2, and 0.3)

no.	T (cm^{-1})	AS (cm^{-1})	B (cm^{-1})	SS (cm^{-1})
0	371.5(5)	479.4(4)	521.9(5)	607.4(5)
0.1	364.0(6)	471.6(4)	520.5(7)	606.1(7)
0.2	372.5(7)	477.6(9)	524.2(9)	609.0(4)
0.3	367.8(7)	473.1(8)	524.2(6)	607.1(4)

are shown in the inset of Figure 5b. The pre-edge peak intensity discontinuously increases with increasing Na content from $x = 0$ to 0.3, and the spectral weight of the preedge peak slightly increases, ~3%, from $x = 0$ to 0.3 in $(Tb_{1-x}Na_x)MnO_{3-y}$. The results indicate that the hole concentration in $(Tb_{1-x}Na_x)MnO_{3-y}$ shows a slight increase when the Na content is increased.

Figure 6 depicts the in-phase component (χ') of the ac magnetic susceptibility of $(Tb_{1-x}Na_x)MnO_{3-y}$ ($x = 0$, 0.15, and 0.3). The high-temperature portions of all the $\chi'(T)$ curves were fitted to Curie−Weiss behavior (solid curves in the inset), and the results are listed in Table 2. The Curie constants were converted into effective moments by $\mu_{eff} = 2.83 \times (MC)^{1/2}$, where M is molecular weight and C is Curie constant in units of emu K g^{-1} Oe. Obviously, the effective moments decrease with increasing x simply because of the replacement of Tb^{3+} ions by Na^{+} ions. The well-defined peak at ~45 K, labeled T_{Mn}, in the $\chi'(T)$ plot of the $x = 0.3$ sample is associated with Mn spin ordering,[1] while the magnetic responses associated with T_{Mn} are not clearly present in the $x = 0.15$ and 0 samples. We believe that the oxygen deficiency in the MnO_6 octahedron may weaken the interaction strength between Mn ions and give a high magnetic response signal in an ac susceptibility experiment. This implies that, in this system, oxygen ions are mediated between Mn ions and play an important role in both ferromagnetic (FM) nearest-neighbor (NN) and antiferromagnetic (AFM) next nearest-neighbor (NNN) superexchange (SE) spin interactions.[13,33] The oxygen vacancies not only caused the interaction path to break but also shorten the distance between Mn ions, which implies that the NN interaction is much preferred at higher Na-doping levels. The transition from NNN to NN interactions with increasing Na-doping will create interactions along the two crystallographic directions at an appropriate Na-doping concentration ($x = 0.15$) and become almost similar. That would caused the magnetic structure changes from incommensurate ($x = 0$) to simple commensurate ($x = 0.15$) and then back to incommensurate ($x = 0.3$), and it would also change the T_C value from −12 K ($x = 0$) to −4 K ($x = 0.15$) and to −21 K ($x = 0.3$), as shown in Table 2. Briefly, the competition between the NNN and NN interactions creates an intermediate state at around $x = 0.15$, which brings simple commensurate magnetic structure and higher T_C. Moreover, it also reveals that the anomaly at around 9 K, labeled T_{Tb}, appears only in the undoped sample. Therefore, the substitution of more Na ions on the Tb site will weaken the rare-earth interaction and dilute the average rare-earth moment in each unit cell.

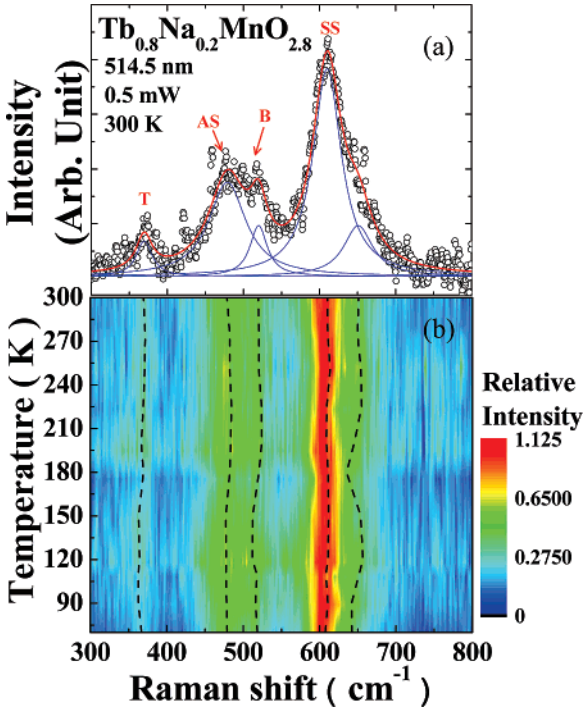

Figure 8. (a) Raman spectra of $(Tb_{1-x}Na_x)MnO_{3-y}$ ($x = 0.2$) at 300 K. (b) Thermal evolution of Raman spectra with fitted peak position (black line).

Raman scattering is an excellent tool for the study of crystal symmetry and its change with doping. The vibration modes allowed in the $RMnO_3$ compounds have been

(33) Kimura, T.; Ishihara, S.; Shintani, H.; Arima, T.; Takahashi, K. T.; Ishizaka, K.; Tokura, Y. *Phys. Rev. B* **2003**, *68*, 060403.

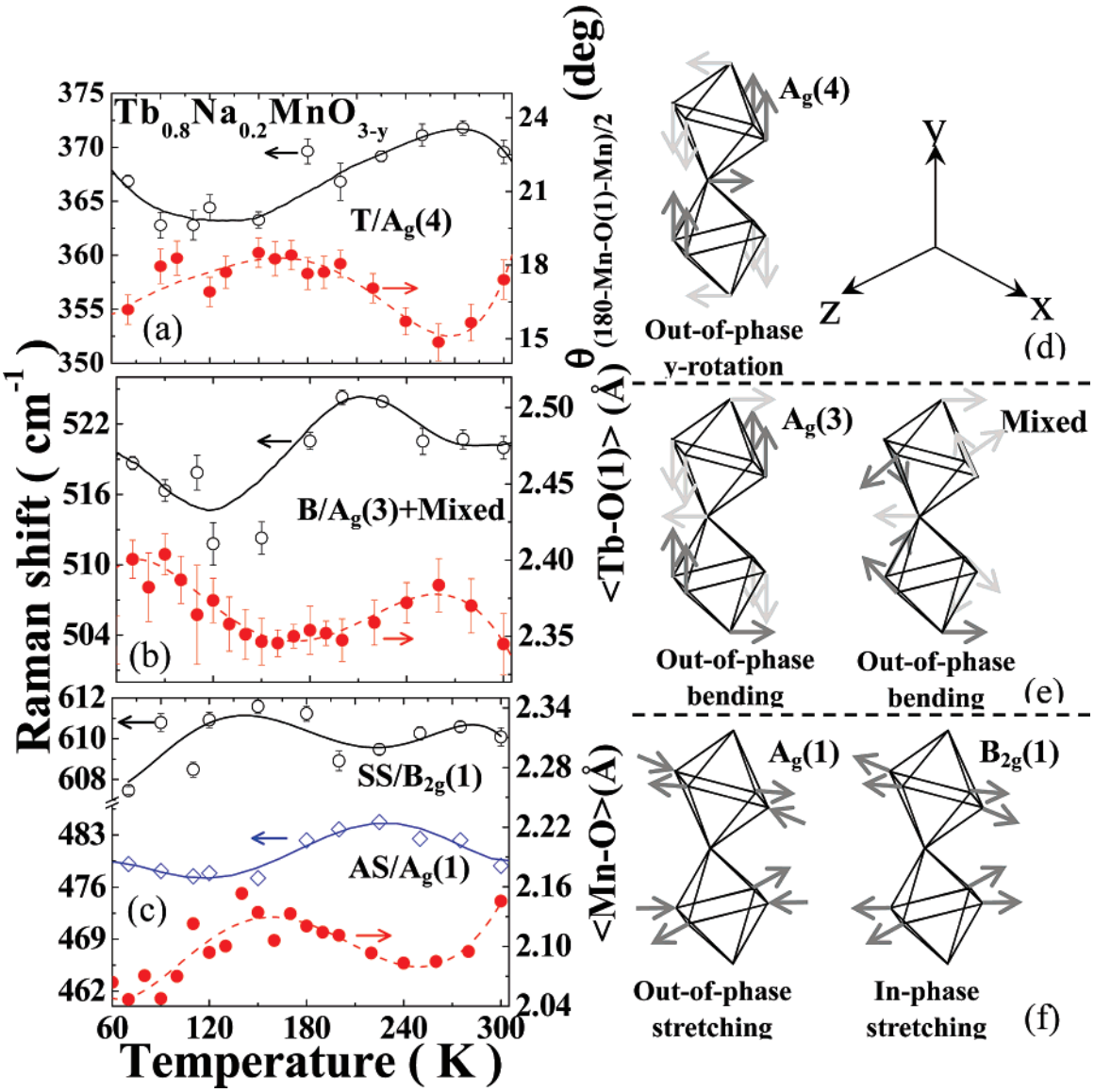

Figure 9. Temperature dependence of Raman frequency of (a) tilt modes, (b) bending modes, and (c) stretching modes for $(Tb_{1-x}Na_x)MnO_{3-y}$ ($x = 0.2$). The X-ray diffraction experiments by refined lattice parameters and some selected bond lengths and angles are give on the right axis for comparison.

idendified.[34−36] For $(Tb_{1-x}Na_x)MnO_{3-y}$, the *Pbnm* symmetry allows 24 active Raman modes of ($7A_g + 7B_{1g} + 5B_{2g} + 5B_{3g}$). Martín-Carrón[35] et al. labeled five observed Raman modes of $RMnO_3$ as R for rare-earth ion mode at ∼250 cm^{-1}, T the tilt, A_g mode at between 280∼370 cm^{-1}, AS for asymmetric stretch A_g mode at around 480 cm^{-1}, B the bending $A_g + B_{1g}$ mode between 420∼530 cm^{-1}, and SS for the symmetric stretch, B_{1g}, around 610 cm^{-1}. Recently, Iliev[37] et al. reported a series of Raman experiments of the single-crystal $RMnO_3$. They pointed out that some normal modes of the Martín-Carrón notation should be corrected. We used Martín-Carrón's notation with Iliev's corrections in this paper. Figure 7a shows the Raman spectrum of $(Tb_{1-x}Na_x)MnO_{3-y}$ ($x = 0$, 0.1, 0.2, and 0.3) samples. Each solid curve sketched on the data points represents the fitted result with a combination of five Lorentz profiles (not shown). The fitting parameters are plotted and listed in Figure 7b and Table 3, respectively. A small perturbation of the peak positions was found as x is increased for T, AS, B, and SS modes, which originate from structural distortion. The Na-doping causes oxygen deficiency and, consequently, the inner structure adjustment, and in turn, it exhibits a peak shift in the Raman spectrum. For the $x = 0.2$ sample, we performed the Raman and X-ray diffraction experiments in temperature-controlled circumstances to study the relation between structure parameters and the Raman mode in detail. Figure 8a depicts the Raman shifts of the $x = 0.2$ sample at 300 K, and Figure 8b shows thermal evolution of the Raman spectra with fitted peak positions (black line). It was found that the sample showed four features labeled as T, AS, B, and SS at around 370, 479, 520, and 610 cm^{-1}, respectively,[35]

(34) Abrashev, M. V.; Bäckström, J.; Börjesson, L.; Popov, V. N.; Chakalov, R. A.; Kolev, N.; Meng, R.-L.; Iliev, M. N. *Phys. Rev. B* **2002**, *65*, 184301-1.
(35) Martín-Carrón, L.; Andrés, A. D; Martínez-Lope, M. J.; Casais, M. T.; Alonso, J. A. *Phys. Rev. B* **2002**, *66*, 174303.
(36) Iliev, M. N.; Abrashev, M. V.; Popov, V. N.; Hadjiev, V. G. *Phys. Rev. B* **2003**, *67*, 212301.
(37) Podobedov, V. B.; Weber, A.; Romero, D. B.; Rice, J. P.; Drew, H. D. *Phys. Rev. B* **1998**, *58*, 43.

and one second-order Raman scattering attributed mainly to the oxygen vibration mode at 650 cm^{-1}.[37] In particular, the trace of all peaks does not shift monotonically as the temperature is increased. It is known that the T, AS, B, and SS modes depend on the Mn−O(1)−Mn angle, Mn−O length, Mn−O length, and Tb−O(1) length, respectively. For comparison, the temperature dependence of the Raman frequencies of the (a) tilt mode, (b) bending modes, and (c) stretching modes for the $x = 0.2$ sample are given in Figure 9. These parameters were obtained from Lorentz fitting of Raman spectrum and X-ray refinement by the GSAS program. From the feature near 370 cm^{-1} (as seen in Figure 9a), which is assigned as T/A_g(4) normal mode (Figure 9d), it is clear that the peak is highly dependent on the tilt angle between the two octahedra as the temperature changes. It is interesting that the opposite evolution curve is present between the tilt angle and Raman shift as the temperature was varied, which is different from Martín-Carrón's[35] report. They replaced the R ion with a bigger one which makes a smaller tilt angle and also presses the octahedra (chemical pressure), which implies that the system needs more energy to drive this mode. In our case, tilt angle changes are only caused by the various temperatures so that it is easier to drive (thermal energy 1 K, ∼0.083 meV, Raman shift 1 cm^{-1}, ∼0.124 meV), while the tilt angle is larger and the peak appears at a smaller Raman shift position. In Figure 9b and e, the bending mode which is assigned as B/A_g(3) + mixed (∼520 cm^{-1}) includes two different A_g(3) normal modes. This indicates that, inside the MnO_6 octahedron, the angle between the O(1)−Mn−O(1) axis (almost along the *c* axis) and the Mn−O(2) plane is bent (as shown in Figure 9d), and the mixed modes are a combination of the A_g(3) and A_g(1) modes. It is easy to understand that a shorter Tb−O(1) bond length will bend the octahedron and bring about a larger force constant, indicating that higher frequency excitation is needed. Moreover, Figure 9c reveals the relation between Mn−O length and both AS/A_g(1) (∼480 cm^{-1}) and SS/B_{2g}(1) peaks (∼610 cm^{-1}). The stretching mode includes symmetric and antisymmetric stretching, which vibrates along Mn−O bonds in- or out-of-phase. The in-phase term of most kinds of vibration motions depend on shorter bond lengths/force constants, and the out-of-phase term is the opposite. This is also in agreement with the sketch in Figure 9c. The observation of these non-monotonically contracting bond lengths and angles with decreasing temperature originated from the balance of ion bonding, asymmetric structure, and defects in the system.

4. Conclusions

The crystallographic and magnetic properties of perovskite-related $(Tb_{1-x}Na_x)MnO_{3-y}$ compounds in the compositional range of $0 \leq x \leq 0.3$ are reported. We demonstrate that the oxygen deficiency in $(Tb_{1-x}Na_x)MnO_{3-y}$ plays an important role in controlling the crystal structure and magnetic properties. An increase in the Na content leads to a reduction in the octahedral distortion and JT effect. Moreover, we found that the oxygen vacancies not only caused the interaction path to break but also caused the distance between Mn ions to shorten, which implies that the NN interaction is preferred at higher Na-doping levels.

Acknowledgment. We thank the National Science Council of Taiwan under Grant 95-2113-M-002-009 and the Ministry of Economic Affairs of Taiwan under Grant 95-EC-17-A-08-S1-0006 for financial support.

IC070190F